applied sciences

MDPI

Article

Experimental Investigation in Drag Coefficient of Cubes

Juanjuan Wang [1,2], Yue Zhang [1,*], Huabing Miao [2], Jiajia Niu [3], Daishu Cheng [4] and Mingzhu Chen [1]

[1] Key Laboratory of Inlet and Exhaust System Technology, Nanjing University of Aeronautics and Astronautics, Ministry of Education, Nanjing 210016, China; juanjuan_wang@nuaa.edu.cn (J.W.); sz2302150@nuaa.edu.cn (M.C.)
[2] AECC Sichuan Gas Turbine Establishment, Mianyang 621000, China; miaohuabing@163.com
[3] Hunan Aviation Powerplant Research Institute, Aero Engine Corporation of China, Zhuzhou 412000, China; wawa_new@163.com
[4] Zhengde Polytechnic, Nanjing 211106, China; fzdso26@126.com
* Correspondence: y.zhang@nuaa.edu.cn

Abstract

Focused on the needs of an accurate drag model for non-spherical particles, a free settling experiment was performed in this paper using the uniformed cube and spliced cube. The drag coefficient of the cube with typical orientation angles at different Reynolds numbers is obtained. The results show that the drag coefficient of the cube is always higher than that of the sphere in the same Reynolds number (*Re*), especially in the range of $Re > 2.58 \times 10^2$. The orientation angle has different effects on the drag coefficient of the cube in different Reynolds number ranges. The drag coefficient of the cube is in direct proportion to its orientation angle in the range of $10 < Re < 10^3$. Then, a new correlation for the drag coefficient of the cube is brought forward. The drag correlation model shows a good agreement with the experimental data as well as the data reported in previous studies.

Keywords: drag coefficient; cube; settling orientation angle; drag model; separation devices design

check for updates

Academic Editor: Ricardo Castedo

Received: 11 May 2025
Revised: 12 June 2025
Accepted: 17 June 2025
Published: 22 June 2025

Citation: Wang, J.; Zhang, Y.; Miao, H.; Niu, J.; Cheng, D.; Chen, M. Experimental Investigation in Drag Coefficient of Cubes. *Appl. Sci.* **2025**, *15*, 7025. https://doi.org/10.3390/app15137025

Copyright: © 2025 by the authors. Licensee MDPI, Basel, Switzerland. This article is an open access article distributed under the terms and conditions of the Creative Commons Attribution (CC BY) license (https://creativecommons.org/licenses/by/4.0/).

1. Introduction

When sand or dust is ingested in the turbine engine, the engine may suffer highly damaging erosion, and the engine life is thus reduced significantly [1]. As a result, sand and dust separation devices are necessary for the turbine engine operating in sandy areas. When the ingested sand or dust particles move in the separation devices, the major interacting force between the air and particles is viscous drag [2]. The degree of turning and acceleration or deceleration achieved by the particles depends on the ratio of the viscous forces to the inertial forces experienced by the particles [3]. Thus, the accurate drag characteristics of sand or dust particles are very important for the separation device's design. Since spherical particles have the simplest geometry to describe, the researchers focused on spherical particles in early studies. Significant work has been performed by various researchers in this field [4–8]. Many equations have been developed relating the drag coefficient to the Reynolds number for spherical shape particles. A review of theoretical and experimental developments about this issue can be found in Clift's book [9]. In combination with abundant numerical and experimental results, the so-called standard

drag curve has been presented, which is accurate in the range of $0.1 < Re < 3 \times 10^5$. Clift's empirical formula is defined as follows:

$$C_D = \frac{24}{Re}\left(1 + 0.15Re^{0.687}\right) + \frac{0.42}{1 + 4.25 \times 10^4 Re^{-1.16}}. \quad (1)$$

Clift's standard drag curve is used directly to predict the particle motion in many separation device designs. However, the prediction of particle motion characteristics may cause significant error since the feature of particles in nature has more complex geometry, which will result in different drag coefficients [10]. Therefore, accurate drag models for non-spherical particles remain a critical need. Based on the settling experiment and numerical method, some researchers have been brought out the models to predict drag coefficients of non-spherical particles [3,11–17]. Table 1 exhibits the widely used prediction model. As can be seen, the form of non-spherical particle's drag coefficient models brought by different researchers show significant differences, and the different models involve different shape factors to describe the particles. This can be attributed to two reasons. Firstly, the geometry feature of non-spherical particles is difficult to describe using a simple uniform factor. Secondly, the secondary motion of the particle leads to variation in the orientation angle as well as the drag coefficient of non-sphere particles during the free-settling process. The secondary motion of the non-spherical particles is inevitable when the Reynolds number is greater than 10 during its free-settling process [18]. These effects lead to the different fitting of drag coefficients. As a result, although the drag models for non-spherical particles greatly improve the prediction of the particle's drag coefficient, the accuracy of them still needs to be improved to satisfy the requirement of practical use. Therefore, in order to improve the accuracy of drag models, the relationship between the drag coefficient and particle orientation angles should be investigated, and the experiment data of non-spherical particles with different fixed orientation angles in a wide Reynolds number range is needed.

The cube is a typical non-spherical particle with a regular shape. The drag characteristics of cubic particles are representative of non-spherical particles, and their settling behavior is crucial for establishing drag coefficient prediction models for non-spherical particles [19]. Some researchers have investigated the relationship between the orientation angle and drag coefficient by using the cube. Wang et al. investigated the sedimentation characteristics of cuboids with a square base [20]. Agarwal and Chhabra investigated the settling behavior of the cube in both Newtonian and Power law liquids [21]. Delidis and Stamatoudis found the velocity of spheres was always greater than that of the cubes with the equal volume in the accelerating region with very high Reynolds number [22]. With the help of numerical methods, Richter and Nikrityuk studied the drag coefficient of the cubic particle at different orientation angles in the range of $10 \leq Re \leq 2 \times 10^2$ [23]. However, the investigation of the relationship between the cube drag coefficient with different settling orientation angles and Reynolds numbers is still limited, especially when the Reynolds number is larger than 2×10^2.

The existing experimental studies on cubic particles primarily use homogeneous materials, which fail to suppress unsteady motions during settling and struggle to measure drag coefficients at specified orientation angles. To address this, we conducted free-settling experiments using non-uniform spliced cubes to stabilize orientation angles and reduce unsteady motions. This approach enabled precise measurements of drag coefficients at typical orientation angles across a wide Reynolds number range. Based on the experimental data, we analyzed the relationship between the cube's drag coefficient, orientation angle, and particle Reynolds number, and developed a reliable correlation to predict the drag coefficient for cube.

Table 1. Widely used prediction model for drag coefficient of non-spherical partials.

Ref.	Prediction Model
Sabine et al. [11]	$C_D = \frac{24}{Re}\frac{d_A}{d_n}\left[1+\frac{0.15}{\sqrt{c}}\left(\frac{d_A}{d_n}Re\right)^{0.687}\right]+\frac{0.42\left(\frac{d_A}{d_n}\right)^2}{\sqrt{c}\left[1+4.25\times10^4\left(\frac{d_A}{d_n}Re\right)^{-1.16}\right]}$, where $c=\pi d_A/P_p$.
Haider and Levenspiel [12]	$C_D = \frac{24}{Re}\left[1+e^{2.3288-6.4581\phi+2.4486\phi^2}Re^{0.0964+0.5565\phi}\right]+\frac{e^{4.905-13.8944\phi+18.4222\phi^2-10.2599\phi^3}Re}{Re+e^{1.4681+12.2584\phi-20.7322\phi^2+15.8855\phi^3}}$,
Swamee and Ojha [13]	$C_D = 0.84\left[\frac{33.78}{(1+4.5\beta^{0.35})^{0.7}Re^{0.56}}+\left(\frac{Re}{Re+700+1000\beta}\right)^{0.28}\frac{1}{(\beta^4+20\beta^{20})^{0.175}}\right]^{1.428}$, where $\beta=\frac{C}{\sqrt{AB}}$.
Ganser [14]	$\frac{C_D}{K_2} = \frac{24}{ReK_1K_2}\left[1+0.1118(ReK_1K_2)^{0.6567}\right]+\frac{0.4305}{1+\frac{3305}{ReK_1K_2}}$, where $K_1=\left(\frac{1}{3}+\frac{2}{3}\phi^{-0.5}\right)^{-1}-2.25\frac{d_n}{D}$ for isometric particles.
	$K_1=\left(\frac{1}{3}\frac{d_A}{d_n}+\frac{2}{3}\phi^{-0.5}\right)^{-1}-2.25\frac{d_n}{D}$ for non-isometric particles.
	$K_2=10^{1.8148(-\log\phi_1)0.5743}$.
Chien [15]	$C_D=\frac{30}{Re}+\frac{67.289}{e^{5.030\phi}}$.
Yow et al. [16]	$C_D=\frac{15.21+\frac{10.82}{\phi}-\frac{0.14}{\phi^2}}{Re}+\frac{13.41-\frac{10.64}{\phi}-\frac{0.06}{\phi^2}}{\sqrt{Re}}-8.82+\frac{5.70}{\phi}+\frac{0.23}{\phi^2}$.
Hölzer and Sommerfeld [17]	$C_D=\frac{8}{Re}\frac{1}{\sqrt{\phi_{II}}}+\frac{16}{Re}\frac{1}{\sqrt{\phi}}+\frac{3}{\sqrt{Re}}\frac{1}{\phi^{3/4}}+0.42\times10^{0.4(-\log\phi)^{0.2}}\frac{1}{\phi_\perp}$.
Bagheri and Bonadonna [3]	$\frac{C_D}{K_2}=\frac{24}{Re}\frac{K_1}{K_2}\left(1+0.125\left(Re\frac{K_2}{K_1}\right)^{2/3}\right)+\frac{0.46}{1+5330/\left(Re\frac{K_2}{K_1}\right)}$, where K_1 and K_2 is the same as the Ganser [14].

2. Experimental Facility and Procedure

The experiment was performed in a vertical rectangular column which is made of transparent plexiglass, as shown in Figure 1a. The column was a rectangular tank with dimensions of 400 mm × 400 mm in length and width, respectively. According to the research of Miyamura [24], when the ratio of the cross-sectional area of the particles to the cross-sectional area of the sedimentation container is less than 0.05, the effect of the wall can be neglected. In this study, this ratio was controlled to be less than 0.0025, thus the influence of the wall on the settlement could be disregarded. Referenced from [19], the height of the tank was chosen to be 1500 mm, which is 75 times the particle characteristic length. The recording area is selected in the position between 800 mm and 1000 mm below the liquid surface, ensuring that the particle velocity is stable and that this position is far from the bottom surface, thus not being affected by the container's bottom boundary. The settling velocity was measured by HX-3 high-speed camera (manufactured by NAC Corporation, Kanagawa, Japan) because of its precise timing. The camera provides the image with a resolution of 1152 × 1896 pixel at 500 frames per second. After calibration with a calibration board, 1 mm of actual length is equivalent to 5 pixels in the captured images. We developed relevant code to achieve automated tracking and the velocity calculation of moving particles captured by a high-speed camera. The code determines the centroid position of particles in each image, where the particle velocity is calculated as the ratio of centroid displacement to the time interval between two consecutive images. The total height of the experimental shooting area is approximately 200 mm. If the shooting area is divided into four speed measurement sections, then the height of each speed measurement section is 50 mm. In the

image, there is an uncertain value of 1 pixel point at this height, which is converted to an actual height of 0.2 mm. Therefore, the error in speed caused by the image resolution is (0.2 mm/50 mm) × 100% = 0.4%. The test results will only be deemed valid if the velocity difference in particles between the first half and the second half of the capture area remains less than 5% and v_p is the average of the two values.

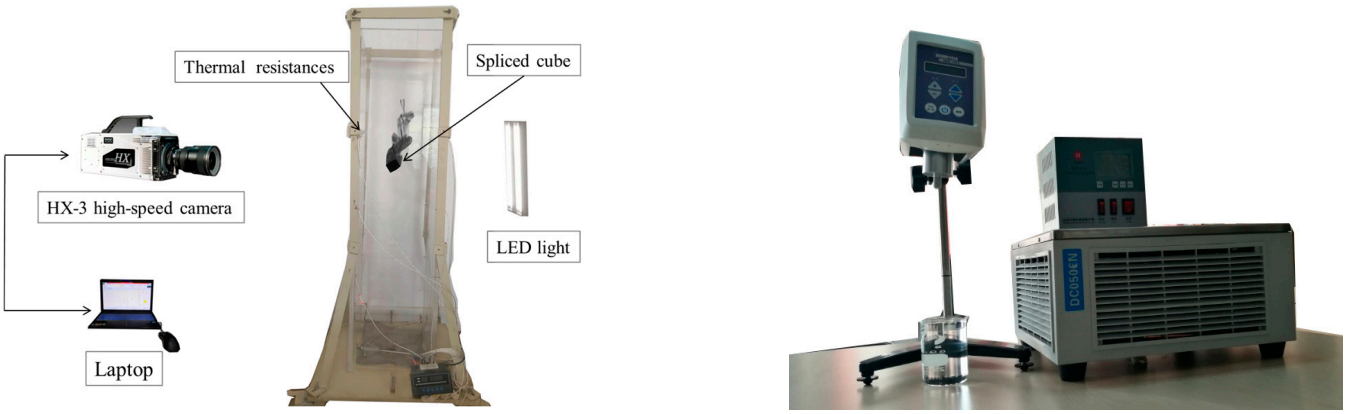


Figure 1. Experimental setup. (**a**) Experimental measurement system. (**b**) Brookfield DVS+ spindle viscometer.

A LED light was used as backlight to illuminate the test section. The LED light was installed with a white semitransparent glass diffuser to achieve a uniform white background. Particles were released beneath the free liquid surface without any air bubble to attach and were as close to the center of the tube as possible. A wire basket was placed near the bottom of the tube to retrieve the particles periodically. Since the temperature has a strong function of viscosity, four sets of twelve thermal resistances were arranged vertically on each side of the tank to monitor the temperature of the fluid during the experiment. Moreover, another moveable thermal resistance was used to record the room temperature and that of the center of the fluid. The temperature gradient over the tube will affect the results. To avoid errors arising due to this reason, a fan was blowing in the direction of the column to ensure the uniformity of the air temperature. Every run of the experiment was carried out within two hours to eliminate the effect of room temperature fluctuation.

Water–glycerine mixtures of various concentrations were used as test liquids to cover a wide range of particle Reynolds numbers. The percentages of glycerine used to define the specific mixtures were determined by volume. The kinematic viscosity of every mixture was measured by a DVS+ spindle viscometer (manufactured by Brookfield, New York, NY, USA; as shown in Figure 1b) under the temperature encountered during the experiment. The accuracy of the viscometer was guaranteed within ±1% of the full-scale range of the spindle/speed combination in use, and it had been calibrated using viscosity standard fluids. The specific gravity of the fluid was measured by a float-type hydrometer. The temperature and specific gravity were measured regularly during the experiment to ensure that the properties of the fluid have not been changed. The mixture of water and glycerine was stirred by a large mixer for at least 10 min to obtain a uniform solution. The fluid was loaded into the tube and kept static for 24 h before the experiment to allow small air bubbles to escape. As a result, the thermal equilibrium can be reached. During this period, the top end of the fall tube was sealed by a plastic membrane to minimize the evaporation losses in the case of glycerol solutions.

There were two types of cubes used in this investigation. One is the uniform cube which is made by a single material, such as aluminum, brass, steel, and PVC with the density of 2750 kg/m^3, 8300 kg/m^3, 7730 kg/m^3, and 1380 kg/m^3, respectively. The uniform cubes have three geometry types with the side length of 10 ± 0.3 mm, 16 ± 0.3 mm and 20 ± 0.3 mm. The other cubes were spliced into two parts which were made by different materials, as shown in Figure 2. The barycenter of the spliced cube is far away from its geometric center, which can keep the orientation angle constant during the settlement. As a result, a moment of force is formed to suppress the secondary motion of the spliced cube and the drag coefficient with a fixed orientation angle is obtained through the free settling experiment. The information on the geometry features and the material of the spliced cubes are listed in Table 2. All the cubes had smooth surfaces, and surface roughness effects were negligible for the studied Reynolds number range. In order to ensure that the cubes achieve rapid stabilization of their orientation angles during the settling process, the cubes with different configurations have different initial released angles. The initial released angle of uniform cubes and spliced cubes with h/a = 0.5 are $0° \pm 1°$. The spliced cubes with h/a = 0.67 and 1.0 are settled in an initial released angle of $20° \pm 1°$ and $45° \pm 1°$, respectively. The same particle was subjected to the sedimentation experiment under the same conditions for three repetitions to reduce random errors.

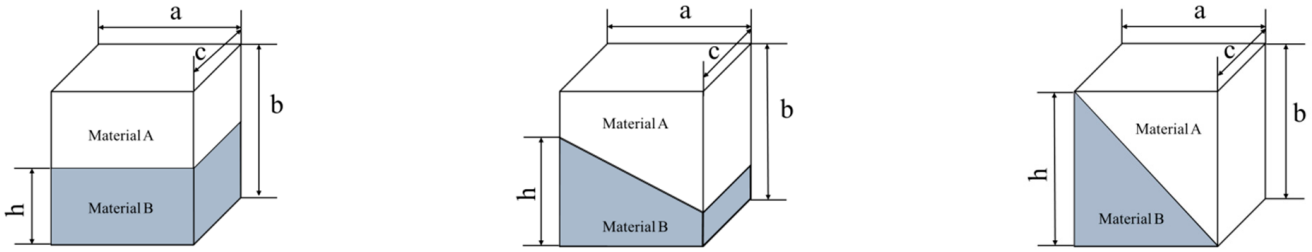


Figure 2. Sketch of spliced cubes.

Table 2. Geometry feature and material of the spliced cubes.

No	*a* (mm)	*b* (mm)	*c* (mm)	*h*/*a*	Material A	Material B	Particle Density (kg/m^3)	Initial Released Angle
1	16.10	16.26	16.08			aluminum	1912.33	
2	16.08	15.98	15.90	0.5		brass	4624	$0° \pm 1°$
3	16.08	16.28	16.10			steel	4394.15	
4	16.24	16.24	16.20			aluminum	1894.18	
5	16.04	16.26	15.92	0.67	PVC	brass	4543.91	$20° \pm 1°$
6	16.10	16.34	16.20			steel	4370.69	
7	16.40	16.38	16.20			aluminum	1877.60	
8	16.30	16.36	16.00	1.0		brass	4534.20	$45° \pm 1°$
9	16.50	16.60	16.30			steel	4199.51	
10	19.92	19.96	20.10			aluminum	1887.18	
11	20.00	19.96	20.10	0.5		brass	4684.99	$0° \pm 1°$
12	20.10	19.92	20.30			steel	4453.89	
13	19.96	20.40	19.92			aluminum	1884.21	
14	20.00	20.40	20.00	0.67	PVC	brass	4648.28	$20° \pm 1°$
15	20.16	20.30	20.26			steel	4352.84	
16	20.16	20.24	19.90			aluminum	1868.11	
17	20.20	20.22	19.96	1.0		brass	4621.75	$45° \pm 1°$
18	20.30	20.18	19.90			steel	4325.75	

Equivalent sphere diameter (d_n), particle Reynolds number (Re_n) are calculated by using Equations (2) and (3), respectively.

$$d_n = \left(\frac{6V_p}{\pi}\right)^{\frac{1}{3}}, \tag{2}$$

$$Re = \frac{\rho_f v_t d_n}{\mu}, \tag{3}$$

where V_p is the volume of particle, d_n is the volume-equivalent sphere diameter. v_t is the terminal velocity

When the particle reaches its terminal velocity, the gravity, buoyancy, and drag are balanced, and the drag can be expressed as follows:

$$F_D = \frac{\pi}{6} {d_n}^3 g(\rho_P - \rho_f). \tag{4}$$

In addition, the drag can also be expressed by using Equation (5):

$$F_D = \frac{\pi}{8} {d_n}^2 C_D \rho_f {v_t}^2. \tag{5}$$

Through Equations (4) and (5), the drag coefficient can be obtained by the following expression:

$$C_D = \frac{4}{3} \frac{g d_n}{{v_t}^2} \left(\frac{\rho_p - \rho_f}{\rho_f}\right), \tag{6}$$

where ρ_p is the density of particle, ρ_f is the density of experimental liquids, and v_t is the terminal velocity.

3. Calibration of Experimental Facility

Several spherical particles with different dimensions and materials shown in Table 3 were used to gauge the overall accuracy and reliability of the experimental methods used in this study. The experimental Reynolds number of the spherical particles is in the range of $2.1 \times 10^{-1} < Re < 8.644 \times 10^3$.

Table 3. Geometry features and materials of the spherical particles.

No	R (mm)	Material	Particle Density (kg/m^3)
1	7.00		
2	12.70	Steel	7730
3	14.30		
4	11.99	Brass	8300

The experimental data and the standard correlation curve presented by Clift were shown in Figure 3. As can be seen, there is an excellent agreement between the experimental data and standard correlation curve brought forward by Clift [9]. The maximum error between the experimental drag coefficients and predicted values using Clift's formula is 3.73%. The Root Mean Square Error (RMSE) is also used to assess the goodness of the fit of the correlations between the experimental and the predictive values. The Root Mean Square Error (RMSE) between the experimental drag coefficients and the predicted ones is 1.94%. This provides high confidence in our present experimental method.

$$\text{RMSE} = \left(\frac{1}{N}\sum_{i=1}^{n}\left(C_{Dn-pre} - C_{Dn-\exp}\right)^2\right)^{\frac{1}{2}}. \tag{7}$$

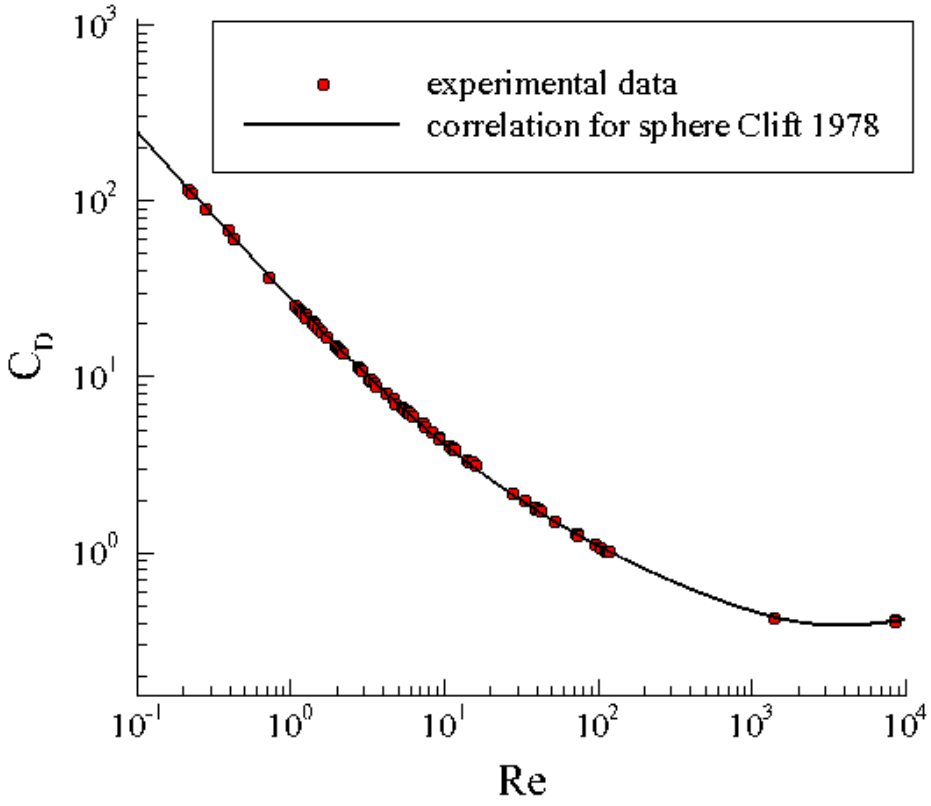


Figure 3. Comparison of experimental sphere drag coefficient and standard correlation of sphere brought forward by Clift [9].

4. Results and Discussion

4.1. Behavior of Uniform Cube Drag Coefficient

The free settling experiment using the uniform cube was performed first. The Reynolds number of particles ranged between 4.75×10^{-1} and 5.7998×10^3 during the experiment. The experimental Reynolds number ranges across the Creeping flow regime where the flow inertia effects are negligible and the flow is laminar; the Transition regime where the flow changes from laminar to turbulent; and the Newton regime where the drag coefficient is roughly constant. Similarly to the former investigations [15], the motion of the uniform cube with noticeable oscillations appears when the particle Reynolds number is larger than a certain value in the Transition regime. In the current investigation, when the Reynolds number is larger than 10, the particle oscillation arises. The experimental drag coefficient of the uniform cube, as well as Clift's standard correlation of the sphere as a function of the Reynolds number, are exhibited in Figure 4. As can be seen, the drag coefficient of the cube is always higher than that of the sphere in the experimental Reynolds range, especially at the range of $Re > 2.58 \times 10^2$. This indicates that the drag coefficient of the cube has its own characteristics which are different from that of the sphere. In addition, the discrete degree of the measured drag coefficient of the cube becomes larger and more complex when the Reynolds number is larger than 10^2, since the settling orientation angle of the cube varies at this Reynolds number range. Therefore, to more accurately characterize the drag coefficient of cubes, further investigation into the effect of orientation angle on cube-shaped particles is necessary.

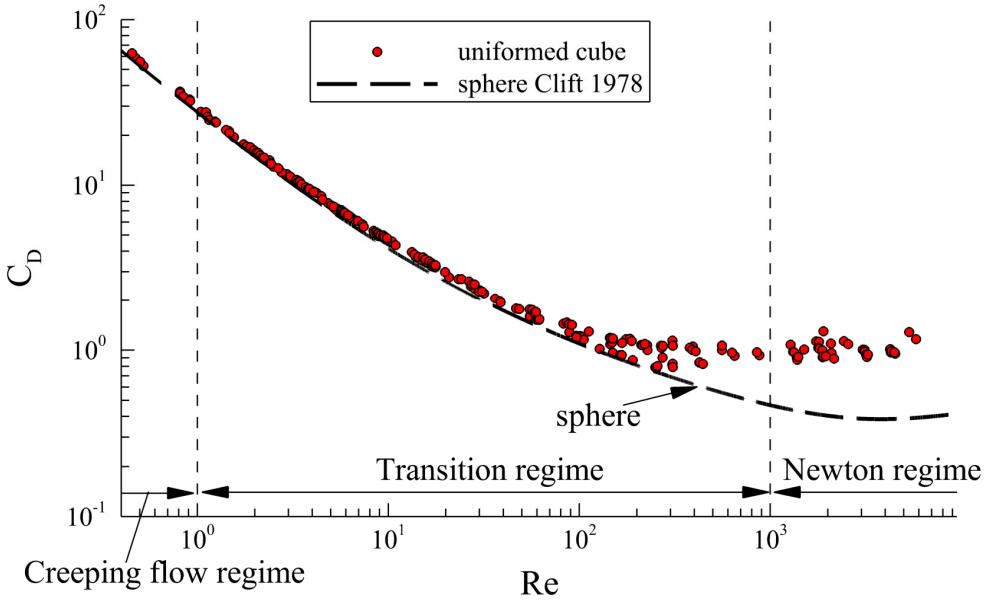


Figure 4. Relationship between drag coefficient and Reynolds number for uniformed cube [9].

4.2. Behavior of the Spliced Cube Drag Coefficient

Then, the free settling experiment is performed by using the spliced cubes. The settling orientation angle of α is defined as the angle of bottom edge of the cube, and the horizontal line on the high speed camera recorded the image, as shown in Figure 5. Therefore, the orientation angle of the cube is within a limit range of $0^\circ \leq \alpha \leq 45^\circ$ during the settling process. When the orientation angle is 0°, the cube has the minimum frontal area. When the orientation angle is 45°, the cube reaches its maximum frontal area during the settling process. For the spliced cubes, the slight secondary motion still exists at a high Reynolds number during its settling process. However, compared with the uniformed cube, the secondary motion amplitude of the spliced cube is suppressed significantly.

Figure 6 exhibits the experimental drag coefficient of the spliced cube with $h/a = 0.5$ and $h/a = 1.0$. The drag coefficient of the sphere is also shown in Figure 6 as a comparison. The experimental Reynolds number, which is in the range of $0.45 \leq Re \leq 4516$, covers the Creeping flow regime, Transition regime, and Newton regime as well. Under the effect of eccentric moments, the spliced cube with $h/a = 0.5$ and $h/a = 1.0$ can maintain the orientation angle around 0° and 45° in the settling process, respectively. Similarly to the uniform cube, the drag coefficient of the spliced cube is always higher than that of the sphere at the same Reynolds number. However, the drag coefficients of different spliced cubes show different variation trends, especially in the range of $10 \leq Re \leq 2.186 \times 10^3$. This indicates that the angle factor has a significant impact on the resistance coefficient of the particles. For the spliced cube with $h/a = 1.0$ and $\alpha = 45^\circ$ the drag coefficient of the cube keeps decreasing as the Reynolds number increases. The decreasing ratio of the drag coefficient is also reduced as the Reynolds number increases. However, the decreasing ratio of the spliced cube with $h/a = 1.0$ is smaller than that of the sphere as Re > 10. As a result, the drag coefficient of the spliced cube with $h/a = 1.0$ is significantly higher than that of the sphere. The variation trend of the drag coefficient of the spliced cube with $h/a = 0.5$ and $\alpha = 0^\circ$ also shows different characteristics with the sphere. The drag coefficients of the cube with $h/a = 0.5$ keep decreasing as the Reynolds number increases in the range of $1 < Re < 2.5 \times 10^2$. Then, the drag coefficient shows an increasing trend in the range of $2.50 \times 10^2 < Re < 2.186 \times 10^3$. The value of the drag coefficient of the spliced cube is close to that with $h/a = 1.0$ at the same Reynolds number when $Re < 10$. Then, the value of the drag coefficient of the spliced cube with $h/a = 0.5$ is smaller than that with $h/a = 1.0$ in the

range of $10 < Re < 10^3$. Finally, the drag coefficient of the two spliced cubes is similar to each other again in the Newton regime.

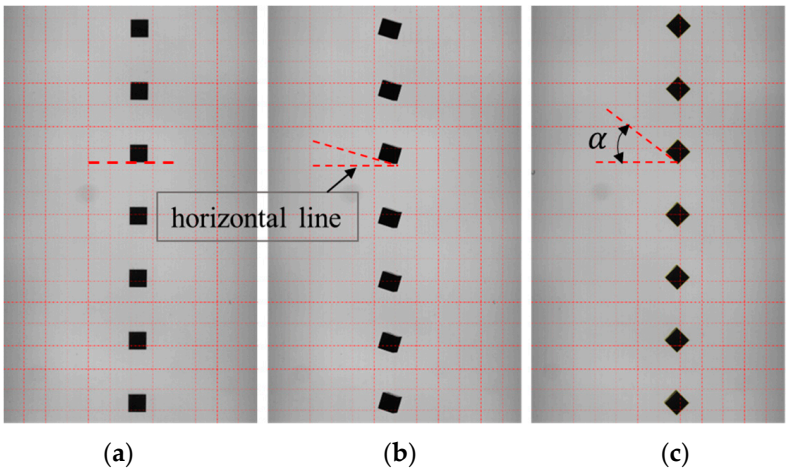


Figure 5. Stable settlement state of three spliced cubes. (**a**) $\alpha = 0°$, $Re = 165.91$; (**b**) $\alpha = 20°$, $Re = 0.91$; (**c**) $\alpha = 45°$, $Re = 112$.

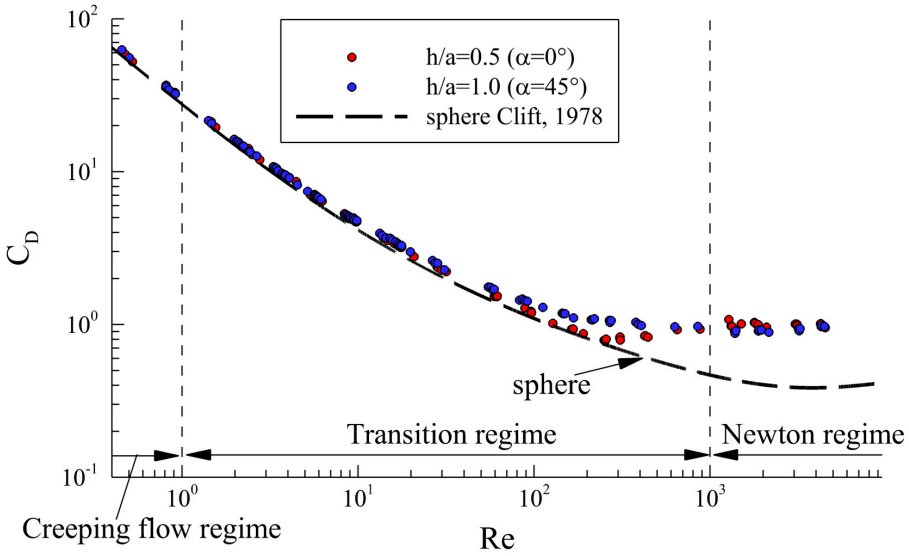


Figure 6. Relationship between drag coefficient and Reynolds number of a spliced cube with $h/a = 0.5$ and 1.0 [9].

For the spliced cube with $h/a = 0.67$, the eccentric moment makes the cube drop in an unsymmetrical incline, which will be affected by the significant lateral force of the fluid. As a result, the orientation angle of the spliced cube with $h/a = 0.67$ is more easily changed compared to the two other cubes with $h/a = 0.5$ and 1.0 during the settling process. Figure 7 exhibits the relationship between the orientation angle and Reynolds number for the spliced cube with $h/a = 0.67$, obtained by the experimental data. As can be seen, the orientation angle of the cube varies along with the Reynolds number. The mean orientation angle of the cube is 16.52° and the standard deviation is 6.076. When the Reynolds number is smaller than 55, the orientation angle of the spliced cube with $h/a = 0.67$ can maintain a stable range of $18.41 \pm 2°$. Then, the orientation angle keeps decreasing till the Reynolds number reaches 1×10^3 and the minimum value of the orientation angle is 2.43°. When the Reynolds number is larger than 1×10^3, the orientation angle keeps increasing and the maximum orientation angle reaches 39°.

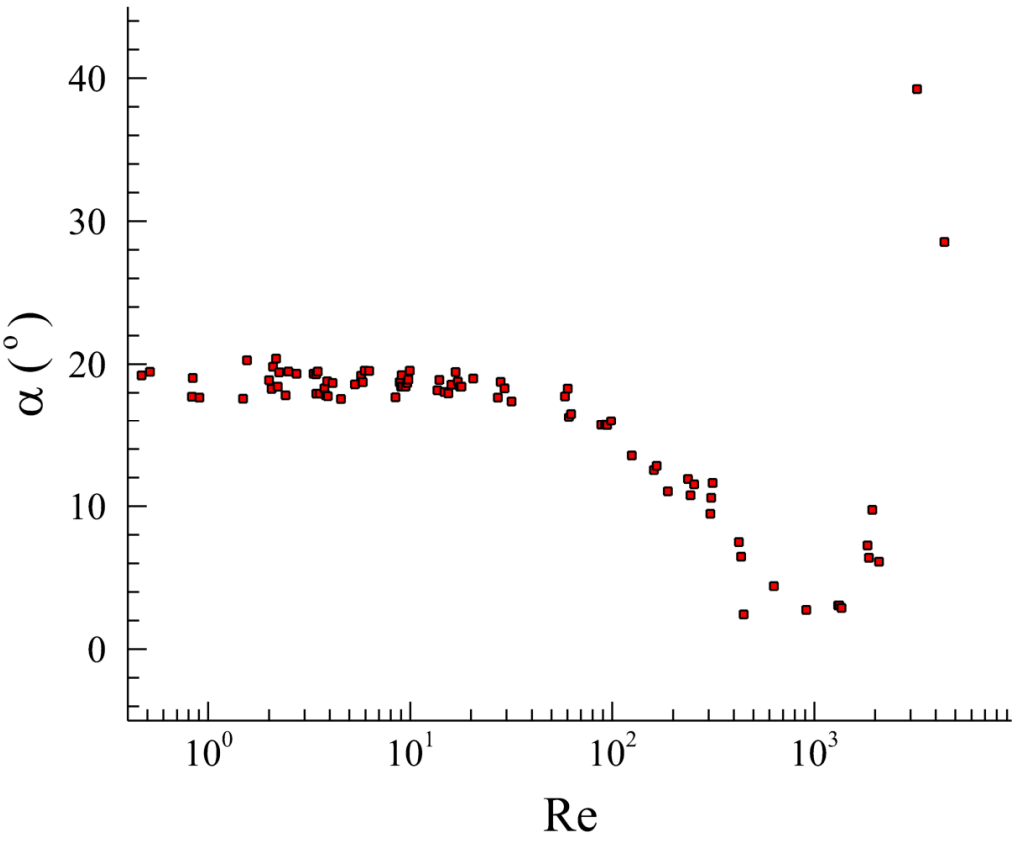


Figure 7. Relationship between orientation angle and Reynolds number of a spliced cube with $h/a = 0.67$.

The experimental drag coefficient of the cube with $h/a = 0.67$ is exhibited in Figure 8. The drag coefficient of the cube with $h/a = 0.5$ and $h/a = 1.0$ is also shown in Figure 8 as a comparison. Since the orientation angle of the spliced cube with $h/a = 0.67$ varies in different Reynolds number ranges, the drag coefficient of the cube is expressed as triangle symbols filled with different colors in the range of $4 \times 10^{-1} < Re < 10$, $10 < Re < 1 \times 10^3$ and $1 \times 10^3 < Re < 4.5 \times 10^3$ in Figure 8, respectively. As can be seen, when the Reynolds number is smaller than 10, the drag coefficients of three types of spliced cubes are very close to each other in the same Reynolds number, indicating that the orientation angle has little effect on the drag coefficient in this Reynolds number range. As the Reynolds number increases to the range of $10 < Re < 1 \times 10^3$, the value of the drag coefficient of the spliced cube with $h/a = 0.67$ is slightly higher than the value of the cube with $h/a = 0.5$ while both of the values are smaller than those of the cube with $h/a = 1.0$. Since the orientation angle of the spliced cube with $h/a = 0.67$ decreases and is finally close to 0° as the Reynolds number increases, the drag coefficient error between the cubes with $h/a = 0.67$ and with $h/a = 0$ keeps decreasing, and they nearly overlap with each other in this Reynolds number range. Compared with the drag coefficients of the spliced cube in Figure 6, the drag coefficient of the cube in this Reynolds number range is in direct proportion to the orientation angle. As a result, the upper and lower bound of the cube drag coefficient in this Reynolds number range are those obtained by the cube with $h/a = 1.0$ ($\alpha = 45^\circ$) and $h/a = 0.5$ ($\alpha = 0^\circ$), respectively. When the Reynolds number is larger than 1×10^3, the effect of the orientation angle on the drag coefficient decreases again. The drag coefficients obtained by different cubes converge with each other once again as the Reynolds number increases.

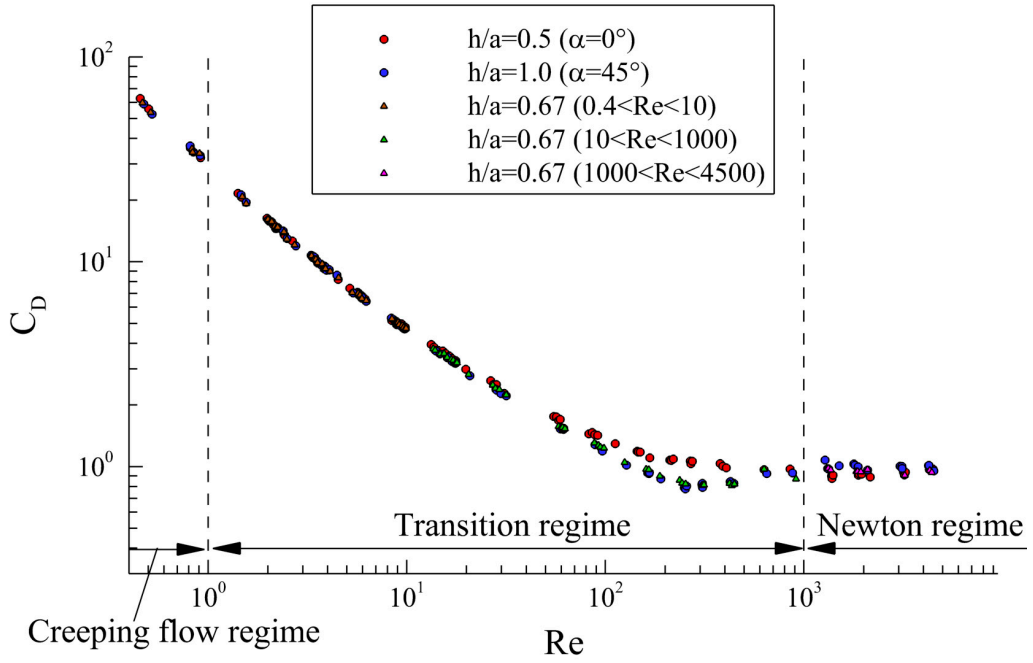


Figure 8. Relationship between drag coefficient and Reynolds number of spliced cubes with h/a = 0.5, 0.67, and 1.0.

4.3. Universal Drag Model for the Cube

According to the above discussion, the orientation angle will have diverse effects on the drag coefficient at different Reynolds number ranges. Therefore, it is a better way to build the drag model for the cube in different Reynolds number ranges. According to the distribution of the drag coefficient of the spliced cubes, the drag model is built in three Reynolds number ranges, which are $0.4 < Re < 10$, $10 < Re < 1 \times 10^3$, and $1 \times 10^3 < Re < 4.516 \times 10^3$. Checking the several forms of drag coefficient models, the most accurate correlation would be obtained by modifying Haider's model [12]. The following expression of the drag coefficient in this paper is expressed as follows:

$$C_D = \frac{24}{Re}(1 + p_1 Re^{p_2}) + \frac{p_3 Re^{p_4}}{Re + p_5}. \quad (8)$$

The parameters p_1, p_2, p_3, p_4, and p_5 are constant values in different Reynolds number ranges.

Table 4 exhibits the value of parameters of Equation (8) in different Reynolds number ranges. Since the orientation angle has little effect on the drag coefficient of the cube in the ranges of $0.4 < Re < 10$ and $1 \times 10^3 < Re < 4.516 \times 10^3$, the drag coefficient of the cube in these two ranges can be expressed by a single expression. The variation trend of the drag coefficients of the cube is quite complex in the range of $10 < Re < 1 \times 10^3$. However, the drag coefficient of the cube is in direct relation to its orientation angle in this range. Thus, the upper and lower boundary of the drag coefficients of the cube in this Reynolds number range can be obtained. The upper bound of the drag coefficient is that with $\alpha = 45°$, while the lower bound of the drag coefficient is that with $\alpha = 0°$.

The comparisons between the experimental drag coefficients for the cube and the predictions from Equation (8) in the range of $0.4 < Re < 4.516 \times 10^3$ are shown in Figure 9. As can be seen, the predications based on Equation (8) fit the experimental data well. The RMSE between the prediction and the experimental data are only 0.25 and 0.048 in the ranges of $0.4 < Re < 10$ and $10^3 < Re < 4.516 \times 10^3$, respectively. In the range of

$10 < Re < 1 \times 10^3$, the RMSE between the prediction and the experimental data with $\alpha = 0°$ and $\alpha = 45°$ are 0.038 and 0.036, respectively.

Table 4. Value of parameters of Equation (8) in different Reynolds number ranges.

Re		p_1	p_2	p_3	p_4	p_5
$0.4 < Re < 10$		−0.02	−3.633	3.907	0.754	−0.378
$10 < Re < 1 \times 10^3$	upper bound ($\alpha = 45°$)	0.213	0.653	0.05	1.344	152.85
	lower bound ($\alpha = 0°$)	0.249	0.586	0.06	1.416	818.921
$1 \times 10^3 < Re < 4.516 \times 10^3$		0.338	0.145	0.669	1.044	−0.002

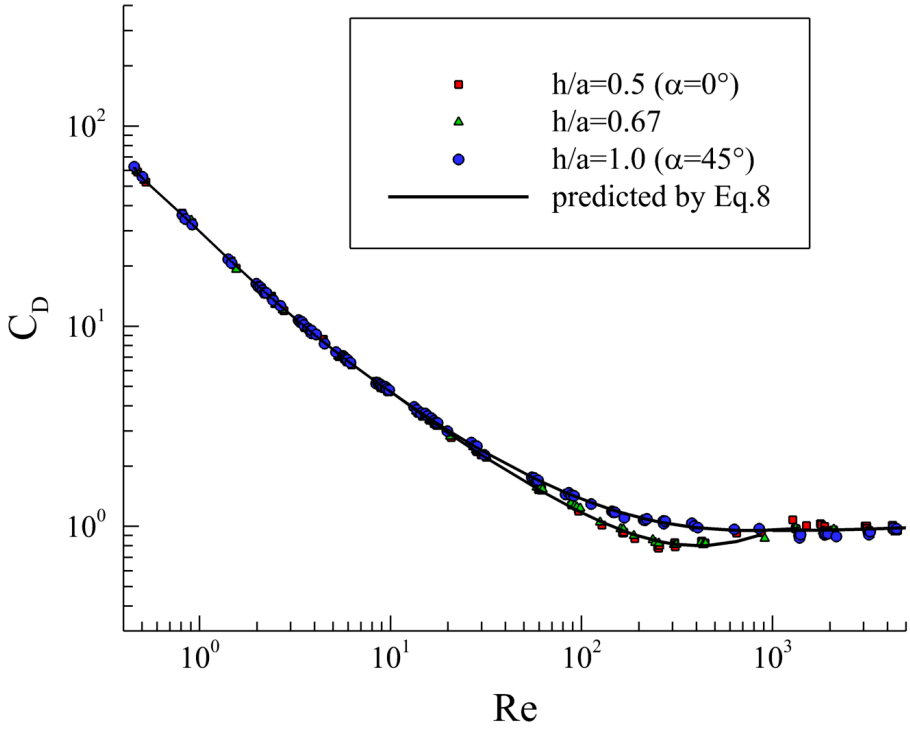


Figure 9. Comparison between the experimental drag coefficients and predictions from Equation (8).

Figure 10 exhibits the distributions of the drag coefficients predicted by Equation (8) and the drag coefficients of the cube obtained by different investigations [20,23–26] as well as that obtained by the uniformed cubes in the current investigations. The results of the drag coefficient correction models brought forward by former investigations [11,12,14,17] are also shown in Figure 10. As can be seen, all the correction models can reflect the variation in the drag coefficient. However, each model has its respective characteristics. The prediction of Sabine's correction [11] is always lower than the measured data, while Ganser's correction [14] is higher than the measured one. In the range of $0.4 < Re < 10$, both Haider's [12] and Holzer's corrections [17] are very close to each other and show good accuracy to the experimental data. However, the prediction of Haider's correction is higher than the experimental data, while Holzer's correction is lower than the experimental data at a high Reynolds number. The prediction in the current paper shows a better agreement with the drag coefficients of the cubes. When the Reynolds number is smaller than 10, the drag coefficients of the cube show a continuous decreasing trend, and Equation (8) predicates the trend with high accuracy. The RMSE between the prediction values from Equation (8) and the drag coefficients of the cube is 0.73 in this Reynolds number range.

Then, in the range of $10 < Re < 1 \times 10^3$, the drag coefficient of the cube shows a significant discreteness, since the orientation angle of the cube plays an important role in its drag coefficient. However, the upper and lower bound of the drag coefficients of the cube in this Reynolds number range are predicted properly. When the Reynolds number is larger than 1000, the prediction values of Equation (8) also fit the drag coefficients of the cube well. The RMSE between the prediction values from Equation (8) and the drag coefficients of the cube is 0.18 in this Reynolds number range.

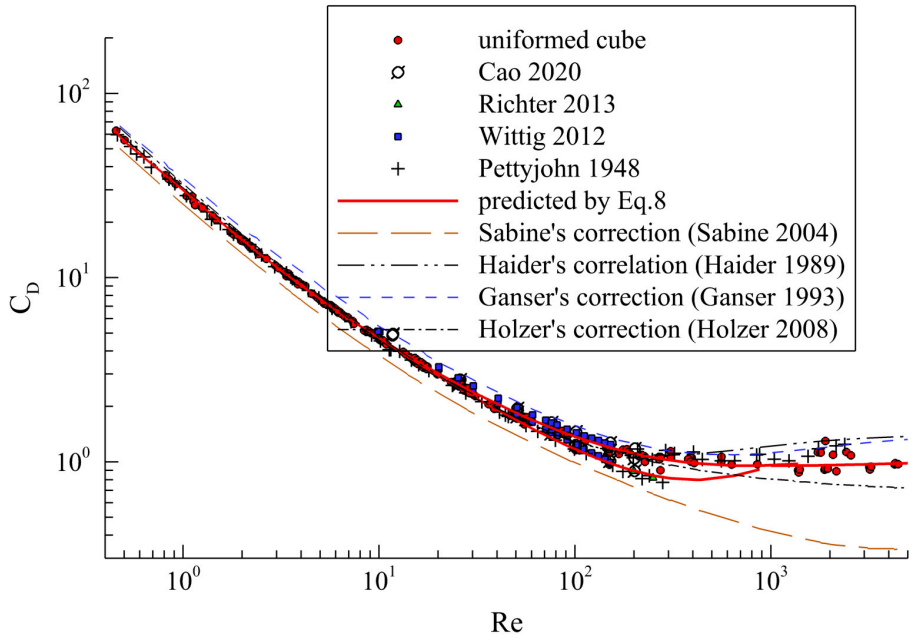


Figure 10. Compression between the predicted drag coefficients by Equation (8) and cube drag coefficients in the previous works [10–12,14,17,23,25,26].

5. Conclusions

This study performed free settling experiments with uniform and spliced cubes to characterize the relationship between drag coefficients and both Reynolds number and orientation angles, revealing several important findings on the effects of orientation angle on drag coefficients.

The drag coefficient of the cube is always higher than that of the sphere in the same Reynolds number, especially at the range of $Re > 258$. When the Reynolds number is larger than 100, the discrete degree of the drag coefficient obtained by the uniformed cube free settling becomes larger and more complex. This is because the orientation angle of the cube varies significantly during the free settling process when the Reynolds number is larger than 100.

The non-uniformed spliced cube can maintain a stable orientation angle in experiment conditions under the effect of the eccentric moment. In particular, the orientation angle of the spliced cube with $h/a = 0.5$ and $h/a = 1.0$ can be maintained at 0° and 45° in a range of $4.5 \times 10^{-1} \leq Re \leq 4.516 \times 10^3$, respectively. According to the experimental data, the orientation angle has different effects on the drag coefficient of the cube in different Reynolds number ranges. When the Reynolds number is in the range of $Re < 10$ and $Re > 1 \times 10^3$, the orientation angle has little effect on the drag coefficient of the cube. While the Reynolds number is in the range of $10 < Re < 1 \times 10^3$, the drag coefficient of the cube is in direct proportion to its orientation angle. The upper and lower bound of the cube drag coefficient in this Reynolds number range is that obtained by the cube with the orientation angle of 45° and that with the orientation angle of 0°, respectively. Based on the

characteristic behaviors of the drag coefficient observed in this study, we propose a new simple yet accurate piecewise correlation model for cube drag coefficients. The correlation model is a piecewise function with a similar form in three Reynolds number ranges, which are $0.4 < Re < 10$, $10 < Re < 1 \times 10^3$ and $1 \times 10^3 < Re < 4.516 \times 10^3$. The drag correlation model shows a good agreement with the experimental data as well as the data reported in previous studies.

Author Contributions: Conceptualization, Y.Z.; investigation, J.W., H.M., J.N., D.C. and M.C.; methodology, Y.Z. and H.M.; formal analysis, J.W., H.M. and J.N.; project administration, Y.Z.; supervision, Y.Z. and D.C.; Validation, J.N. and M.C.; writing—original draft, J.W.; writing—review and editing, D.C. and M.C. All authors have read and agreed to the published version of the manuscript.

Funding: This study was supported by the National Science and Technology Major Project J2019-II-0014-0035 and Defense Industrial Technology Development Program GJCZ-0102-2024-0005.

Institutional Review Board Statement: Not applicable.

Informed Consent Statement: Not applicable.

Data Availability Statement: The data within the article can be made available upon request.

Conflicts of Interest: Authors Juanjuan Wang and Huabing Miao were employed by the company AECC Sichuan Gas Turbine Establishment and Author Jiajia Niu was employed by the company Aero Engine Corporation of China. The remaining authors declare that the research was conducted in the absence of any commercial or financial relationships that could be construed as a potential conflict of interest.

Nomenclature

Re	particle Reynolds number
Cd	the drag coefficient
a,b,c	edge length of a cube
h	thickness of Material B
V_p	the volume of particle
d_n	the volume-equivalent-sphere diameter
d_A	the surface-equivalent sphere diameter
P_p	the projected perimeter of the particle in its direction of motion
A	maximum dimension of particle
B	intermediate dimension of particle
C	minimum dimension of particle
D	model parameters
ϕ	sphericity
ρ_p	the density of particle
ρ_f	the density of experimental liquids
v_t	the terminal velocity
RMSE	The Root Mean Square Error
α	the orientation angle
p_1, p_2, p_3, p_4	model parameters

References

1. Hamed, A.; Tabakoff, W.; Wenglarz, R. Erosion and Deposition in Turbomachinery. *J. Propuls. Power* **2006**, *22*, 350–360. [CrossRef]
2. Filippone, A.; Bojdo, N. Turboshaft engine air particle separation. *Prog. Aerosp. Sci.* **2010**, *46*, 224–245. [CrossRef]
3. Bagheri, G.; Bonadonna, C. On the Drag of Freely Falling Non-Spherical Particles. *Powder Technol.* **2016**, *301*, 526–544. [CrossRef]
4. Brown, P.P.; Lawler, D.F. Sphere drag and settling velocity revisited. *J. Environ. Eng.-ASCE* **2003**, *129*, 222–231. [CrossRef]
5. Turton, R.; Levenspiel, O. A short note on the drag correlation for spheres. *Powder Technol.* **1986**, *47*, 83–86. [CrossRef]

6. Concha, F.; Barrientos, A. Settling velocities of particulate systems, 3. Power-series expansion for the drag coefficient of a sphere and prediction of the settling velocity. *Int. J. Miner. Process.* **1982**, *9*, 167–172. [CrossRef]
7. Almedeij, J. Drag coefficient of flow around a sphere: Matching asymptotically the wide trend. *Powder Technol.* **2008**, *186*, 218–223. [CrossRef]
8. Cheng, N. Comparison of formulas for drag coefficient and settling velocity of spherical particles. *Powder Technol.* **2009**, *189*, 395–398. [CrossRef]
9. Clift, R.; Grace, J.R.; Weber, M.E. *Bubbles, Drops and Particles*; Academic Press: New York. NY, USA, 1978.
10. Cao, Z.; Tafti, D.K.; Shahnam, M. Development of drag correlation for suspensions of ellipsoidal particles. *Powder Technol.* **2020**, *369*, 298–310. [CrossRef]
11. Sabine, T.; Gay, M.; Michaelides, E.E. Drag coefficients of irregularly shaped particles. *Powder Technol.* **2004**, *139*, 21–32.
12. Haider, A.; Levenspiel, O. Drag coefficient and terminal velocity of spherical and non-spherical particles. *Powder Technol.* **1989**, *58*, 63–70. [CrossRef]
13. Swamee, P.K.; Ojha, C.S.P. Drag coefficient and fall velocity of nonspherical particles. *J. Hydraul. Eng.* **1991**, *117*, 660–667. [CrossRef]
14. Ganser, G.H. A rational approach to drag prediction of spherical and nonspherical particles. *Powder Technol.* **1993**, *77*, 143–152. [CrossRef]
15. Chien, S.F. Settling velocity of irregularly shaped particles. *SPE Drill. Complet.* **1994**, *9*, 281–289. [CrossRef]
16. Yow, H.N.; Pitt, M.J.; Salman, A.D. Drag correlations for particles of regular shape. *Adv. Powder Technol.* **2005**, *16*, 363–372. [CrossRef]
17. Hölzer, A.; Sommerfeld, M. New simple correlation formula for the drag coefficient of non-spherical particles. *Powder Technol.* **2008**, *184*, 361–365. [CrossRef]
18. Rosendahl, L. Using a multi-parameter particle shape description to predict the motion of non-spherical particle shapes in swirling flow. *Appl. Math. Model.* **2000**, *24*, 11–25. [CrossRef]
19. Wang, J.; Qi, H.; Zhu, J. Experimental study of settling and drag on cuboids with square base. *Particuology* **2011**, *9*, 298–305. [CrossRef]
20. Richter, A.; Nikrityuk, P.A. Drag forces and heat transfer coefficients for spherical, cuboidal and ellipsoidal particles in cross flow at sub-critical Reynolds numbers. *Int. J. Heat Mass Transf.* **2012**, *55*, 1343–1354. [CrossRef]
21. Agarwal, N.; Chhabra, R.P. Settling velocity of cubes in Newtonian and Power law liquids. *Powder Technol.* **2007**, *178*, 17–21. [CrossRef]
22. Delidis, P.; Stamatoudis, M. Comparison of the velocities and the wall effect between spheres and cubes in the accelerating region. *Chem. Eng. Commun.* **2009**, *196*, 841–853. [CrossRef]
23. Richter, A.; Nikrityuk, P.A. New correlations for heat and fluid flow past ellipsoidal and cubic particles at different angles of attack. *Powder Technol.* **2013**, *249*, 463–474. [CrossRef]
24. Miyamura, A.; Iwasaki, S.; Ishii, T. Experimental Wall Correction Factors of Single Solid Sphere in Triangular and Square Cylinders, and Parallel Plates. *Int. J. Multiph. Flow* **1981**, *7*, 41–46. [CrossRef]
25. Wittig, K.; Richter, A.; Nikrityuk, P.A. Numerical Study of Heat and Fluid Flow Past a Cubical Particle at Sub-Critical Reynolds Numbers. In Proceedings of the ICHMT International Symposium on Advances in Computational Heat Transfer, Bath, UK, 1–5 July 2012.
26. Pettyjohn, E.S.; Christiansen, E.R. Effect of particle shape on freesettling rates of isometric particles. *Chem. Eng. Prog.* **1948**, *44*, 157–172.

Disclaimer/Publisher's Note: The statements, opinions and data contained in all publications are solely those of the individual author(s) and contributor(s) and not of MDPI and/or the editor(s). MDPI and/or the editor(s) disclaim responsibility for any injury to people or property resulting from any ideas, methods, instructions or products referred to in the content.